



## RESEARCH ARTICLE

10.1029/2023GC011338

### Key Points:

- Aphyric rhyolite eruptions staged from shallow magma reservoirs lack the overpressure needed for homogeneous bubble nucleation
- Heterogeneous bubble nucleation may occur on sub- $\mu\text{m}$  titanomagnetite crystals, which are undetectable using standard analytical techniques
- Sub- $\mu\text{m}$  titanomagnetite crystals can be detected and quantified with low temperature magnetic analyses

### Supporting Information:

Supporting Information may be found in the online version of this article.

### Correspondence to:

K. N. McCartney,  
[kmccartn@hawaii.edu](mailto:kmccartn@hawaii.edu)

### Citation:

McCartney, K. N., Hammer, J. E., Shea, T., Brachfeld, S., & Giachetti, T. (2024). Evaluating the role of titanomagnetite in bubble nucleation: Novel applications of low temperature magnetic analysis and textural characterization of rhyolite pumice and obsidian from Glass Mountain, California. *Geochemistry, Geophysics, Geosystems*, 25, e2023GC011338. <https://doi.org/10.1029/2023GC011338>

Received 7 NOV 2023

Accepted 2 FEB 2024

### Author Contributions:

**Conceptualization:** Julia E. Hammer, Thomas Shea, Stefanie Brachfeld, Thomas Giachetti

**Funding acquisition:** Julia E. Hammer, Thomas Shea, Stefanie Brachfeld

**Investigation:** Kelly N. McCartney, Julia E. Hammer, Thomas Shea, Stefanie Brachfeld, Thomas Giachetti

**Methodology:** Kelly N. McCartney, Julia E. Hammer, Thomas Shea, Stefanie Brachfeld, Thomas Giachetti

# Evaluating the Role of Titanomagnetite in Bubble Nucleation: Novel Applications of Low Temperature Magnetic Analysis and Textural Characterization of Rhyolite Pumice and Obsidian From Glass Mountain, California

Kelly N. McCartney<sup>1</sup> , Julia E. Hammer<sup>1</sup>, Thomas Shea<sup>1</sup> , Stefanie Brachfeld<sup>2</sup> , and Thomas Giachetti<sup>3</sup> 

<sup>1</sup>University of Hawaii at Manoa, Honolulu, HI, USA, <sup>2</sup>Montclair State University, Montclair, NJ, USA, <sup>3</sup>University of Oregon, Eugene, OR, USA

**Abstract** Nucleation of H<sub>2</sub>O vapor bubbles in magma requires surpassing a chemical supersaturation threshold via decompression. The threshold is minimized in the presence of a nucleation substrate (heterogeneous nucleation, <50 MPa), and maximized when no nucleation substrate is present (homogeneous nucleation, >100 MPa). The existence of explosively erupted aphyric rhyolite magma staged from shallow (<100 MPa) depths represents an apparent paradox that hints at the presence of a cryptic nucleation substrate. In a pair of studies focusing on Glass Mountain eruptive units from Medicine Lake, California, we characterize titanomagnetite nanolites and ultrananolites in pumice, obsidian, and vesicular obsidian (Brachfeld et al., 2024, <https://doi.org/10.1029/2023GC011336>), calculate titanomagnetite crystal number densities, and compare titanomagnetite abundance with the physical properties of pumice to evaluate hypotheses on the timing of titanomagnetite crystallization. Titanomagnetite crystals with grain sizes of approximately 3–33 nm are identified in pumice samples from the thermal unblocking of low-temperature thermoremanent magnetization. The titanomagnetite number densities for pumice are 10<sup>18</sup> to 10<sup>20</sup> m<sup>-3</sup>, comparable to number densities in pumice and obsidian obtained from room temperature methods (Brachfeld et al., 2024, <https://doi.org/10.1029/2023GC011336>). This range exceeds reported bubble number densities (BND) within the pumice from the same eruptive units (average BND  $\sim 4 \times 10^{14}$  m<sup>-3</sup>). The similar abundances of nm-scale titanomagnetite crystals in the effusive and explosive products of the same eruption, together with the lack of correlation between pumice permeability and titanomagnetite content, are consistent with titanomagnetite formation having preceded the bubble formation. Results suggest sub-micron titanomagnetite crystals are responsible for heterogeneous bubble nucleation in this nominally aphyric rhyolite magma.

## 1. Introduction

Vesiculation in magmas is initiated by the nucleation of bubbles in response to a progressive decrease in the solubility of volatiles (e.g., H<sub>2</sub>O, CO<sub>2</sub>, S) during decompression. However, bubbles do not nucleate instantaneously because energy is required to create an interface between the exsolved fluid and silicate liquid (Mangan & Sisson, 2000). The existence of this energy barrier means that there is generally a lag between attainment of a volatile saturation pressure and the formation of bubbles (usually termed the supersaturation pressure  $\Delta P_N$ ; e.g., Mourtada-Bonnefoi & Laporte, 2002). The supersaturation pressure may be reduced if nucleation is assisted by a solid substrate (heterogeneous nucleation), and otherwise high if no such energy reducing agent is present (homogeneous nucleation). When occurring early during magma ascent, heterogeneous nucleation of bubbles on existing crystals ultimately fosters efficient degassing (Mangan & Sisson, 2000). This swift response of gas exsolution to decompression maintains the system closer to melt-gas equilibrium (Figure 1). Late homogeneous nucleation unaided by crystals delays degassing until shallow levels, at which point degassing occurs abruptly, increasing the likelihood of explosive fragmentation (Mangan & Sisson, 2000). Differences in nucleation style and timing can therefore result in drastically different magma ascent and eruption scenarios.

Both homogeneous and heterogeneous nucleation suffer from observational inconsistencies. The large supersaturation pressure required for homogeneous nucleation ( $\Delta P_N > 150$  MPa for high silica magmas; Hurwitz & Navon, 1994; Klug et al., 2002; Mourtada-Bonnefoi & Laporte, 2002) prescribes magma storage depths of >6 km

© 2024 The Authors. *Geochemistry, Geophysics, Geosystems* published by Wiley Periodicals LLC on behalf of American Geophysical Union.

This is an open access article under the terms of the [Creative Commons Attribution License](https://creativecommons.org/licenses/by/4.0/), which permits use, distribution and reproduction in any medium, provided the original work is properly cited.

**Project administration:** Julia E. Hammer, Stefanie Brachfeld

**Supervision:** Julia E. Hammer, Thomas Shea, Stefanie Brachfeld

**Writing – original draft:** Kelly N. McCartney, Julia E. Hammer, Thomas Shea, Stefanie Brachfeld, Thomas Giachetti

**Writing – review & editing:** Kelly N. McCartney, Julia E. Hammer, Thomas Shea, Stefanie Brachfeld, Thomas Giachetti

assuming a lithostatic pressure gradient (i.e., storage pressure needs to exceed  $\Delta P_N$ ). However, some Plinian eruptions involving rhyolite magma were fed by magma stored at pressures between 50 and 150 MPa (2–6 km), too low or barely sufficient for homogeneous nucleation to take place (determined by Classical Nucleation Theory, Hirth et al. (1970); summarized in Shea (2017)). Examples of shallow to moderate storage depths for the reservoirs supplying magma to large explosive eruptions include Novarupta 1912 CE (1.8–4.1 km depth, 13–14 km<sup>3</sup> DRE, dense rock equivalent; Coombs & Gardner, 2001), Askja 1875 CE (~5 km depth, 0.2 km<sup>3</sup> DRE; Clark, 2012), Crater Lake 7.7ka (~5 km depth, 60 km<sup>3</sup> DRE; Buckland et al., 2020), and Taupo ~180 CE (6–8 km depth, 18 km<sup>3</sup> DRE; Dunbar & Kyle, 1993). Heterogeneous nucleation on crystal substrates occurs at much lower  $\Delta P_N$  (<50 MPa) and seems more likely for magmas stored at these shallow depths (Shea, 2017). However, the magmas feeding many large-scale rhyolitic eruptions are crystal-poor, thus lacking obvious substrates for heterogeneous bubble nucleation. For heterogeneous nucleation to dominate in crystal-poor rhyolites, the numeric abundance of crystals should be similar to typical bubble number densities (BND) (Cáceres et al., 2020), which are on the order of  $10^{14}$ – $10^{17}$  m<sup>-3</sup> (Shea, 2017). The apparent absence of sufficient numbers of crystals in many silicic eruptions could be due to the detection limits of conventional observational methods (e.g., petrographic microscope, X-ray tomography) and/or 2D sectioning effects (Sahagian & Proussevitch, 1998; Shea, 2017; Shea et al., 2010). Optimal conditions with X-ray tomography yield approximately 0.5–1  $\mu$ m per voxel resolution, and subsample a volume less than 9 mm<sup>3</sup>, severely limiting the ability to detect sub- $\mu$ m sized particles, especially in highly porous materials such as pumice. Electron microscopy can reach sub- $\mu$ m resolution but is limited to 2D observations. Alternative means of detecting sub- $\mu$ m particles are available for magnetic minerals. For example, Wörm and Jackson (1999) used low-temperature magnetic measurements on the Yucca Mountain Tuff to quantify the abundance of superparamagnetic (sub- $\mu$ m) titanomagnetite through their remanence behavior.

Titanomagnetite is a common and early-forming mineral phase in silicic magmas (Butler, 1992). Titanomagnetite aids bubble nucleation by lowering the melt-vapor interfacial energy, and therefore the  $\Delta P_N$  required for bubble nucleation to  $\leq 25$  MPa through its influence on the melt-vapor interfacial energy (Cluzel et al., 2008; Gardner & Denis, 2004; Hurwitz & Navon, 1994). It is possible that in crystal-poor magmas, titanomagnetite crystals are present at the nanometer scale, undetectable by petrographic means, yet enabling heterogeneous bubble nucleation. However, few comparisons between bubble and oxide number densities have been carried out thus far in experimental and natural samples, and they are limited to oxide grains on the order of  $\mu$ m(s) in size (Burgisser et al., 2020; Cluzel et al., 2008; Colombier et al., 2020; Gardner, 2007; Gardner & Denis, 2004; Giachetti et al., 2010; Shea et al., 2010), within the spatial resolving power of petrographic imaging methods. Using magnetic techniques similar to those applied by Wörm and Jackson (1999), we aim to determine the number densities of nanometer-scale titanomagnetite crystals in crystal-poor silicic pumice. A first step in evaluating the role of nm crystals in the eruption process is to compare titanomagnetite number densities (TND) to BND. The next critical step is to evaluate the relative timing of crystal and bubble formation.

In order to influence bubble nucleation, titanomagnetite formation has to precede magma ascent. Determining the timing of titanomagnetite's appearance during the eruptive sequence is challenging. If the majority of titanomagnetite particles form late in the magma ascent history, or after tephra deposition, clearly they cannot be involved in catalyzing bubble nucleation. There are at least three mechanisms through which the late titanomagnetite formation can occur. First, tephra that remains hot after deposition in an oxidizing atmosphere can crystallize oxides (Mandeville et al., 1994; Till et al., 2011; Wallace et al., 2002). This problem can be avoided by selecting for analysis only the small (lapilli-sized or smaller) rapidly cooled tephra clasts from fall deposits for analysis rather than coarser pumices from slowly cooled pyroclastic density current deposits (Wörm & Jackson, 1999). Second, exsolution dissociates volatiles such as H<sub>2</sub>O into hydrogen and oxygen. If oxygen were to migrate from the bubble back into the melt (e.g., a retrograde solution reaction; Burgisser et al., 2015; Waters & Lange, 2016), local changes in Fe<sup>3+</sup>/Fe<sup>2+</sup> could stabilize titanomagnetite (Colombier et al., 2020; Rust & Cashman, 2011). Arguing against the viability of this effect is the finding by Waters and Lange (2016) that water exsolution does not change the redox state of the surrounding melt. Titanomagnetite is therefore unlikely to form due to degassing-induced melt oxidation. Third, permeable outgassing and fluxing of oxidizing vapors through an open network could induce the formation of oxides along bubble walls. If titanomagnetite formed after vesiculation, vesicularity and/or permeability would likely correlate with titanomagnetite abundance; the absence of any such textural correlation would be consistent with titanomagnetite formation having preceded vesiculation. In addition, the materials produced by eruptions that span a range of explosive intensities are anticipated to contain similar abundances of titanomagnetite particles, if those crystals formed prior to bubble nucleation. For example,

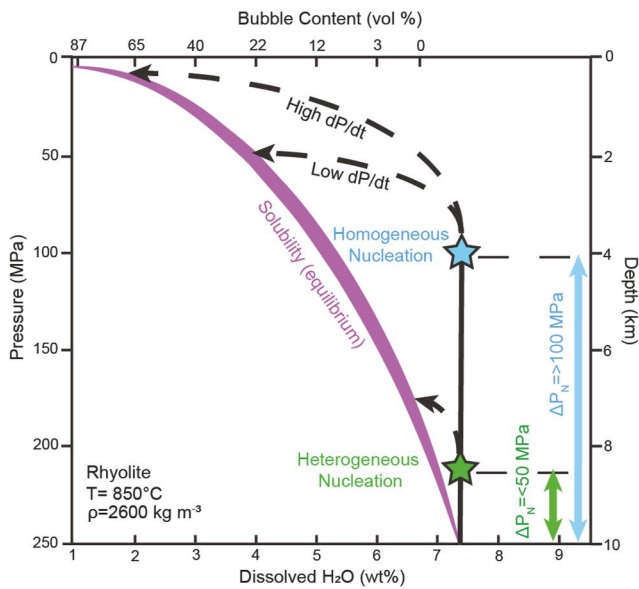


**Figure 1.** Possible degassing paths of water-saturated rhyolite as a function of bubble nucleation mechanism. Water exsolves from the melt into vapor as it ascends to the surface and decompresses. The purple region designates the solubility limit of a rhyolite at 850°C from 250 to 0 MPa. A delay in degassing can be caused by a delay in nucleation as magma decompresses (here shown as the supersaturation pressure required to initiate vesiculation,  $\Delta P_N$ ). The efficiency by which the system returns to equilibrium is determined by the style of nucleation, with homogeneous nucleation (green) allowing the system to track equilibrium conditions better than homogeneous nucleation (blue). Modified from Shea (2017) and Mangan and Sisson (2000).

obsidian and pumice from a given eruption would contain similar titanomagnetite populations, if those populations existed in the deep conduit. The eruptive processes that produced obsidian flows and pumice-forming explosive units at Glass Mountain clearly represent different ascent histories and degrees of outgassing. However, they are inferred to have originated from the same storage reservoir (Heiken, 1978) and thus sample the same “initial” conditions.

Solving the homogeneous versus heterogeneous nucleation debate thus requires (a) a method capable of resolving titanomagnetite at sub- $\mu\text{m}$  resolution, and (b) a parallel investigation to determine the timing of titanomagnetite formation. In a companion paper, we characterize the volume fraction (and volume % (v%)), magnetic domain state (which describes the micron-scale spatial pattern of magnetization within a single grain), and magnetic mineralogy of Glass Mountain (Medicine Lake, CA, USA, 1060 CE; Grove et al., 1997) pumice, obsidian, and vesicular obsidian, and make preliminary estimates of number densities by assuming monospecific grain size assemblages and grain size distributions that follow a power law (Brachfeld et al., 2024). In this study, we apply the Wörm and Jackson (1999), low-temperature remanence-based method for calculating titanomagnetite number density that makes no a priori assumptions about the grain sizes present. We then compare titanomagnetite and BND measured in Glass Mountain subplinian pumice, obsidian, and vesicular obsidian. Finally, using MELTS models and the textural characteristics of vesicles and titanomagnetite in natural pumice and obsidian, we evaluate whether titanomagnetite formation likely preceded bubble nucleation. There are three possible outcomes regarding the relative number densities of crystals and bubbles in the studied pumice: (a) nm-scale titanomagnetite is absent or present with number densities near our minimum detection limit, (b) nm-scale titanomagnetite is present but at number densities below those of the bubbles, and (c) nm-scale

titanomagnetite is present in similar or larger number densities than the bubbles. Outcomes 1 or 2 would support the petrographic assessment that homogeneous bubble nucleation dominates magma degassing, and an alternative explanation for the large differential pressure and disequilibrium required for bubble nucleation is needed. If Case 3 is correct, our assumptions about homogeneous bubble nucleation in the context of the ascent and degassing behavior of aphyric rhyolite systems need to be reevaluated with heterogeneous nucleation in mind.

## 2. Materials and Methods

### 2.1. Sample Selection

In this study, we used nearly crystal-free rhyolitic pumice and obsidian from the 1060 CE Glass Mountain eruption of Medicine Lake Volcano, California, USA (~3% of plagioclase microlites and rare phenocrysts of plagioclase and orthopyroxene; Grove et al., 1997). The Glass Mountain eruption occurred on the eastern rim of the Medicine Lake caldera, producing 1 km<sup>3</sup> volume (DRE) of obsidian flows/domes and fall deposits. The tephra deposits represent the early stages of the eruption, and are dominated by aphyric pumice, with proximal deposits several meters in thickness, thinning to less than 1 cm about 40 km away from the vent (Heiken, 1978). The selected pumice is a high silica rhyolite (74 wt% SiO<sub>2</sub>, Table 1) characterized petrologically by Grove et al. (1997) and examined for residual magmatic water content by Giachetti et al. (2020; 0.2–0.5 wt% H<sub>2</sub>O, Table 1). The obsidian samples come from thick lava flows that traveled down the east flank of the volcano, from the same eruptive center that also produced the tephra deposits. The obsidian flow range in texture from dense and glassy block flows to more vesicular. Dacite magma was involved in the latter stages of the eruption but was ignored for our sampling, which focuses on the earlier rhyolitic phase.

Tephra samples were taken from a quarry located about 2 km northeast of the inferred vent and obsidian flows, where the early explosive phases are easily accessible. Pumice A2,  $B_{\text{max}}$ , and C2 are from the same sample location but from different beds, and pumice-labeled M comes from the same quarry but from a different location

**Table 1**  
*Pumice and Obsidian Glass Geochemistry*

Oxides	Pumice <sup>a</sup> (wt%)	±	Obsidian <sup>b</sup> (wt%)	±
SiO <sub>2</sub>	73.74	0.30	73.62	0.43
TiO <sub>2</sub>	0.28	0.02	0.27	0.02
Al <sub>2</sub> O <sub>3</sub>	14.00	0.06	13.94	0.14
FeO	1.74	0.07	1.71	0.04
MnO	0.03	0.01	0.03	0.01
MgO	0.27	0.03	0.27	0.01
CaO	1.31	0.02	1.3	0.03
Na <sub>2</sub> O	4.20	0.11	4.11	0.11
K <sub>2</sub> O	4.35	0.05	4.35	0.05
P <sub>2</sub> O <sub>5</sub>	0.03	0.03	0.04	0.01
SO <sub>3</sub>	0.01	0.01	0.01	0.01
Cl	0.02	0.02	0.07	0.01
Total	100.03		99.72	
Max H <sub>2</sub> O	0.50 <sup>b</sup>		0.11 <sup>c</sup>	
Min H <sub>2</sub> O	0.20 <sup>b</sup>		0.10 <sup>c</sup>	

<sup>a</sup>Glass compositions determined by EPMA at UH Manoa. <sup>b</sup>Giachetti et al. (2015). <sup>c</sup>Measured by Allan Lerner at the University of Oregon.

University of Oregon; Table 1). Samples of the N. obsidian were cored out of the main clasts into 5-mm-diameter, 70-mm-long cylinders for analysis. Samples of the S. obsidian and S. vesicular flow were sliced into 1 cm pieces. In total, 54 pieces of obsidian were analyzed for this study.

## 2.2. MELTS Modeling

We performed thermodynamic modeling of the saturation conditions of titanomagnetite in Glass Mountain rhyolite using MELTS at 200 MPa, oxygen fugacity ( $fO_2$ ) values corresponding to the FMQ buffer and above, with H<sub>2</sub>O sufficient for near-liquidus saturation of an H<sub>2</sub>O-rich volatile phase (Ghiorso & Gualda, 2015; Gualda et al., 2012). These conditions are consistent with the environment of the rhyolite's genesis, as ascertained by the laboratory experiments of Grove et al. (1997). The pumice and obsidian studied are nearly identical in composition, and the composition of the pumice (Table 1) was used as the starting composition for the MELTS models. The relevant model outputs are the temperature at which the liquid saturates with a spinel-structured phase (titanomagnetite solid solution), and the mass of titanomagnetite crystallized at each temperature step along the isobaric cooling path, calculated in 2-degree increments.

## 2.3. Textural Characterization: Density, Volume, Vesicularity, and Permeability

Characterization of vesicle textures yields information on the vesicularity and permeability of the samples. We quantify the vesicularity of 189 pumice clasts using Archimedes' method (e.g., Houghton & Wilson, 1989; Shea et al., 2010) and helium-pycnometry (e.g., Formenti & Druitt, 2003). In addition, 14 pieces of the S. vesicular obsidian were measured using only Archimedes' method, as total vesicularity and bulk density were necessary for our study. Archimedes' method yields the bulk density of the sample, which can be converted into total vesicularity of the sample using the density of the solid phase (the above-mentioned DRE). Pycnometry provides targeted information about the solid

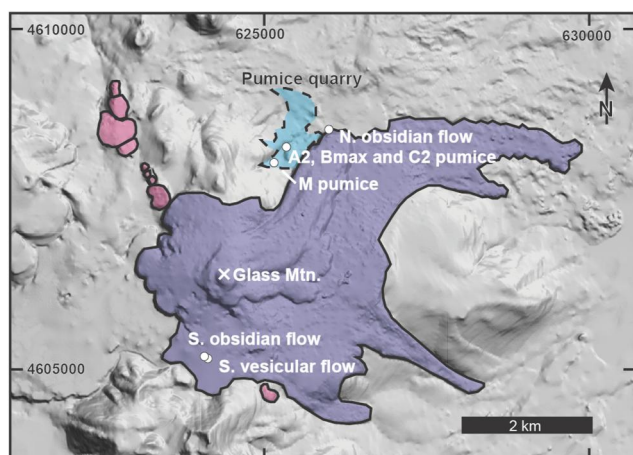


**Figure 2.** Map of the Glass Mountain 1060 CE eruption obsidian flow field (dark blue) and sampling areas. The main vent location is marked by a cross symbol and sample locations are marked by white dots. All pumice samples were collected at the quarry to the north (cyan dashed region). This eruption produced 10 domes (pink), which were not analyzed for this study.

(Figure 2). In total, 210 clasts were analyzed for this study. Bulk rock chemistry is essentially constant between pumice clasts, and there is little difference in vesicularity and permeability among clasts (Table 2). The average DRE density of the pumice determined by pycnometry is 2,390 kg/m<sup>3</sup>. The pre-eruptive water content is estimated to be 4–6 wt% H<sub>2</sub>O (Grove et al., 1997). Pumices with visible fractures were avoided as they could give a misleading permeability reading. In addition, pumice with any yellow/pink coloring was avoided as it may have experienced a longer cooling time and formed secondary sets of oxides after eruption. The average pumice size used for this analysis was 2–3 cm. The average bubble number density of the pumice clasts is on the order of 10<sup>13</sup> to 10<sup>15</sup> m<sup>-3</sup> (Giachetti et al., 2015; Trafton & Giachetti, 2021).

The obsidian samples selected for this analysis come from a northern and southern rhyolite flow lobes and were chosen for their apparently microlite-free glassy character (Figure 2). A glassy block of obsidian was sampled from both northern and southern locations, with an additional vesicular flow block sampled from the southern location (~0.005 m<sup>3</sup> of material from each sample site). Studying both vesicular and dense obsidian allows for a range of textures to be examined. All were formed during the effusive phase of the Glass Mountain eruption, but the vesicular sample provides an opportunity to draw comparisons to the bubble-rich pumice which was formed during the explosive phase, in the context of total vesicularity. The obsidian has a DRE density of 2,430 kg/m<sup>3</sup> (Giachetti et al., 2015) and FTIR measurements yield a total water content of 0.10–0.11 wt% (measured by Allan Lerner at the

**Table 2**  
*Physical Characteristics of Pumice Clasts Used for Magnetic Analysis*

Sample	Statistic	$\phi_T$ (vol%) <sup>a</sup>	$\phi_C$ (vol%) <sup>b</sup>	$\phi_V$ <sup>c</sup>	$\phi_I$ (vol%) <sup>d</sup>	Log( $k_1$ ) (m <sup>2</sup> ) <sup>e</sup>	Log( $k_2$ ) (m) <sup>f</sup>
GMA2	Avg <sup>g</sup>	65.11	77.06	84.29	11.96	-11.63	-7.72
	$\sigma$ <sup>h</sup>	8.14	5.77	6.50	4.73	0.48	0.73
	%rsd <sup>i</sup>	12.5	7.49	7.71	39.56	-4.09	-9.39
	$n$ <sup>j</sup>	78	78	78	78	3	3
GMBmax	Avg	60.73	70.52	85.82	9.79	-	-
	$\sigma$	8.93	6.44	7.56	4.78	-	-
	%rsd	14.70	9.13	8.81	48.84	-	-
	$n$	92	92	92	92	-	-
GMC2	Avg	70.94	78.53	90.39	7.60	-12.05	-8.40
	$\sigma$	2.41	3.15	3.06	2.57	0.37	0.53
	%rsd	3.40	4.01	3.39	33.85	-3.10	-6.28
	$n$	6	6	6	6	6	6
Quarry	Avg	66.12	73.80	89.47	7.68	-12.10	-8.24
	$\sigma$	8.22	6.63	5.96	4.13	0.44	0.50
	%rsd	12.43	8.98	6.67	53.79	-3.64	-6.08
	$n$	10	10	10	10	10	10

<sup>a</sup>Total porosity, measured using Archimedes' method. <sup>b</sup>Connected porosity, measured using pycnometry. <sup>c</sup>Ratio of connected/total porosity (unitless). <sup>d</sup>Isolated porosity, measured using pycnometry. <sup>e</sup>Darcian permeability, measured using permeameter, calculated using the Forchheimer equation. <sup>f</sup>Non-Darcian permeability, measured using permeameter, calculated using the Forchheimer equation. <sup>g</sup>Average value. <sup>h</sup>Standard deviation. <sup>i</sup>Relative standard deviation. <sup>j</sup>Population number.

and isolated pore volume of a sample and therefore its isolated and connected vesicularities. This is an important distinction because only connected vesicularity can contribute to the overall permeability of the clast, whereas isolated vesicles cannot. A summary of the measured vesicularity can be found in Table 2.

Permeability provides a proxy for the efficiency of gas flow within a pyroclast. Like connectivity, permeability can be compared with titanomagnetite abundance to check for covariations. Measured permeability provides information on the efficiency of gas flow within a small parcel of ascending magma, under the assumption that the pyroclastic texture is representative of the magma at fragmentation. Sample preparation and measurement follow the methodologies of Takeuchi et al. (2005, 2008) and Klug and Cashman (1996). Samples (19 total) were cored into cylinders, and the sides sealed with a heat shrinking tube to allow for the permeability to be measured from end to end. These jacketed samples were then hermetically fixed to a plexiglass disc for analysis in a PMI Capillary Flow Porometer at the University of Oregon.

Permeability was calculated using the Forchheimer equation:

$$\frac{P_i^2 - P_o^2}{2P_o L} = \frac{\mu}{k_1} v_0 + \frac{\rho}{k_2} v_0^2 \quad (1)$$

where input pressure is  $P_i$  (Pa), exit pressure is  $P_o$  (Pa),  $L$  is sample length (m),  $\mu$  is fluid dynamic viscosity (Pa.s), and  $v_0$  is air flow velocity (m/s) (Equation 1; Rust & Cashman, 2004). This form allows for the calculation of viscous permeability (Darcian;  $k_1$ ; log m<sup>2</sup>) as well as inertial permeability (non-Darcian;  $k_2$ ; log m) by varying the applied pressure and measuring air flow velocity. A summary of permeability measurements can be found in Table 2.

#### 2.4. Magnetic Measurements

Low-field magnetic susceptibility (the induced magnetization per unit applied field) was measured on 249 samples at Montclair State University, as described in Brachfeld et al. (2024). Each measurement was normalized

by mass and reported as  $\chi$  in units of  $\text{m}^3/\text{kg}$ . Low temperature remanence data for 5 pumice samples and 1 obsidian sample were measured on a Quantum Design Magnetic Properties Measurement System (MPMS-XL) at the Institute for Rock Magnetism, University of Minnesota. In a field cooled-zero field cooled (FC-ZFC) experiment (after Moskowitz et al., 1993), a low temperature remanence was imparted at 5 K after cooling from 300 K in the presence of a 2.5 T field. This is termed a FC experiment and represents a thermoremanent magnetization (TRM, a signal acquired when a sample cools below its blocking temperature in the presence of an ambient magnetic field) for nanoparticles that have blocking temperatures below 300 K. The intensity of remanence was measured during warming to 300 K. The experiment is repeated by cooling from 300 to 5 K in zero applied fields (ZFC, zero-field cooling) and applying a 2.5 T field at 5 K to induce an isothermal remanent magnetization (IRM, a signal acquired by subjecting a sample to a DC field). The intensity of the IRM is then measured during warming to 300 K. This FC-ZFC pair of experiments has been applied to investigate order-disorder transitions, domain state, and blocking volumes in titanomagnetite (Dunlop & Özdemir, 1997; Moskowitz et al., 1993, 1998).

## 2.5. Titanomagnetite Grain Size Distribution and Number Density

We calculate titanomagnetite number density (TND) using the method presented in Wörm and Jackson (1999), which is based on Néel theory (Néel, 1949) and assumes an assemblage of  $N$  particles, identical in shape and composition, and varying only in grain volume ( $v_{\text{particle}}$ ). The number of particles present in a sample is derived from the thermal decay of a low-temperature TRM using the interplay of relaxation time ( $\tau$ ), blocking temperature ( $T_B$ ), and blocking volume ( $V_B$ ). The relaxation time  $\tau$  is the time required for the magnetization of a particle to decay in the absence of an ambient magnetic field, or the time required for the magnetization of a particle to change directions when subjected to an applied magnetic field. When  $\tau$  is short,  $<100$  s (an upper limit for instrumental analyses), changes in magnetization can be manipulated and observed in laboratory experiments. When  $\tau$  is very long, on the order of billions of years, the magnetization is stable and described as “blocked,” yielding familiar magnetizations in igneous rocks that are the basis for plate tectonic reconstructions and other paleomagnetic applications (e.g., Butler, 1992 and references therein).

The relaxation time given by Néel theory depends on temperature according to:

$$\tau = \tau_0 \exp\left(\frac{\mu_0 H_k V M_S}{2kT}\right) \quad (2)$$

where  $\tau_0$  is the pre-exponential frequency factor, with experimentally determined values of  $10^{-8}$  to  $10^{-13}$  s for ferritin, maghemite, and titanomagnetite (Berndt et al., 2015; Dickson et al., 1993; Moskowitz et al., 1997; Wörm & Jackson, 1999),  $\mu_0$  is the permeability of free space and equal to  $1.257 \times 10^{-6} \frac{\text{mkg}}{\text{s}^{-2}\text{A}^{-2}}$ ,  $H_k$  is the microcoercivity of the carrier mineral (calculated as the macrocoercivity  $H_C \times 2.09$  in A/m (Stoner & Wohlfarth, 1948)), which represents the energy barrier to magnetization changes,  $V$  is grain volume,  $M_S$  is saturation magnetization for the carrier mineral in A/m,  $k$  is the Boltzmann constant  $1.38 \times 10^{-23} \frac{\text{m}^2\text{kg}}{\text{s}^2\text{K}}$ , and  $T$  is temperature (K).

At temperatures above  $T_B$ , the energy barrier to changes in magnetization is small,  $\tau$  is short, and even a weak applied magnetic field can produce a net alignment of magnetic moments parallel to the applied field. Upon cooling below  $T_B$ , the energy barrier becomes sufficiently large that the net alignment is preserved and  $\tau$  increases by orders of magnitude, “blocking in” the TRM. While traditional applications of TRM in tectonics and paleomagnetism focus on the magnetic behavior of stable single domain (SSD) and larger grains at and above room temperature, the same relationships between  $\tau$ ,  $T_B$ , and  $V_B$  in Equation 2 also hold for nanoparticles below room temperature.

$T_B$  varies with grain volume. Each  $T_B$  has a corresponding  $V_B$ , the volume above (below) which  $\tau$  rapidly increases (decreases) and energy barriers to magnetization changes rapidly increase (decrease). A sub-micron titanomagnetite grain may exhibit either superparamagnetic behavior (SP,  $\tau < 100$  s) or SSD behavior ( $\tau > 10^9$  years) depending on the combination of particle volume, ambient temperature ( $T$ ) and observation time ( $t$ ). At a given blocking temperature  $T_B$ ,  $V_B$  represents the volume at which a particle transitions from SSD (below  $T_B$ ) to SP behavior (above  $T_B$ ), and represents the condition at which a stable remanence is acquired upon cooling below  $T_B$ . For a given  $v_{\text{particle}}$ , the particle can be forced to exhibit SSD behavior by lowering its temperature below  $T_B$  or

shortening the measurement duration below  $\tau$ , and can be forced to exhibit SP behavior by raising the temperature above  $T_B$  or using a measurement duration longer than  $\tau$ .

Exploiting the interplay between volume, temperature, and time in order to extract particle volume begins with rearranging Equation 2 to solve for the blocking volume and setting  $\tau$  equal to the experimental measurement time ( $\tau_m$ ):

$$V_B = \frac{2kT}{\mu_o H_k M_S} \ln\left(\frac{\tau_m}{\tau_o}\right) \quad (3)$$

We use the term “carrier mineral” to indicate the magnetic mineral composition. We set  $\tau_m$  to 3 s, the measurement time for remanence in the MPMS instrument. We use a  $\tau_o$  value of  $10^{-9} \text{ s}^{-1}$ , consistent with direct observations of Moskowitz et al. (1997) for magnetoferritin, and with Wörm and Jackson (1999) and Berndt et al. (2015) for the Tiva Canyon Tuff. We note that using a smaller value of  $\tau_o$  slightly increases  $V_B$  values by approximately 3.5% and decreases TND by approximately 9% for each order of magnitude, which does not substantially alter the grain size range or the order of magnitude of the TND.

We assign two carrier mineral macrocoercivity ( $H_C$ ) values at 5 K, 10 and 100 mT for all of our samples (which are subsequently converted to  $H_k$  in units of A/m). Low-temperature hysteresis capabilities were not available due to helium supply challenges in Montclair, and the necessary instrumentation was not yet reinstalled during our visit to the Institute for Rock Magnetism following their relocation, necessitating this strategy for  $H_C$ . We selected 10 and 100 mT (approximately 10 and 100 times the room temperature  $H_C$  value) to examine the impacts of  $H_k$  on  $V_B$  and TND. Room temperature  $M_S$  values for the carrier mineral composition are determined from Curie temperature measurements, which are empirically calibrated through compilations of  $M_S$  data for titanomagnetites (Bleil & Petersen, 1982).

To determine the number of grains of each  $v_{\text{particle}}$  present, we calculated the change in magnetic moment ( $\Delta m$ , in units of  $\text{Am}^2$ ) between each successive pair of temperature steps  $T_1$  and  $T_2$  in the FC remanence experiment during warming to 300 K. We solve for the number of particles at each blocking volume  $V_B$  (from Equation 3), defined as the volume bin bounded by  $V_{B(T_1)}$  and  $V_{B(T_2)}$ , required to account for the loss of remanence.

The magnetic moment ( $m$ ) of an individual particle is given by

$$m_{\text{particle}} = v_{\text{particle}} \times M_{S_{\text{carrier mineral}}} \quad (4)$$

The saturation remanent moment ( $m_{rs}$ ) of an assemblage of  $N$  identical particles randomly oriented in the sample and at temperatures below the blocking temperature ( $T < T_B$ ) is given by

$$m_{rs} = 0.5 \times N \times v_{\text{particle}} \times M_{S_{\text{carrier mineral}}} \quad (5)$$

For an assemblage of non-identical particles, the change in moment ( $\Delta m_{rs_i}$ ) between two successive temperature steps is the signal carried by the particles within the blocking volume bin,  $v_i$ , bounded by the two temperatures:

$$\Delta m_{rs_i} = 0.5 \times N_i \times v_i \times M_{S_{\text{carrier mineral}}} \quad (6)$$

where  $v_i$  is the blocking volume given by Equation 3, and the term  $N_i \times v_i$  represents the total volume of the bin.

$M_{S_{\text{carrier mineral}}}$  varies with temperature, represented as  $M_S(T)$ .  $M_S(T)$  is modeled as a Bloch Law below 300 K as per Wörm and Jackson (1999), and given by:

$$M_S(T) = M_S(0 \text{ K}) \times \left(1 - C^{\frac{3}{2}}\right) \quad (7)$$

where  $M_S(0 \text{ K})$  is determined from  $M_S(298 \text{ K})$  for the carrier mineral composition, which in turn is determined from Curie temperature measurements (see Brachfeld et al., 2024), and  $C$  is the Curie Constant (a dimensionless constant of  $10^{-5}$ ).

Using these relationships, the number of particles present in the sample within the  $i$ th blocking volume bin,  $N_i$ , is determined by rearranging Equation 6 and substituting Equations 3 and 7 to obtain:

$$N_i = \frac{2\Delta m_{rs_i}}{v_{B_i} \times M_S(T)} \quad (8)$$

The number of particles per unit volume for each bin is determined by dividing  $N_i$  by the volume of the sample, which is nominally 0.2 mL for the MPMS-XL sample holder:

$$N(V_i) = \frac{2\Delta m_{rs_i}}{v_{B_i} \times M_S(T) \times V_{\text{sample}}} \quad (9)$$

The TND (in units of  $\text{m}^{-3}$  of sample) is the sum of all  $N(V_i)$  determined from the field-cooled remanence experiment. The TND value is adjusted to a vesicle-free basis (i.e., DRE) via the total vesicularity (expressed as volume fraction) according to:

$$\text{TND} = \frac{\sum N(V_i)}{(1 - \phi)} \quad (10)$$

where  $\phi$  = is the total vesicularity. The DRE-adjusted TND value represents the availability of titanomagnetite substrate particles present prior to vesiculation as sites for heterogeneous bubble nucleation.

This method requires the absence of crystallographic order-disorder transitions, for example, the Verwey transition in pure magnetite at 120 K or 50–70 K order-disorder transitions observed in moderate to high-Ti titanomagnetite (Moskowitz et al., 1998) and titanomagnetite with other cation substitutions (Brachfeld & Hammer, 2006), which would cause a large decrease in remanence during warming that is unrelated to blocking volume. Therefore, we restrict this calculation to FC-ZFC samples for which these transitions and multidomain (MD) behavior are absent.

### 3. Results

#### 3.1. Physical Characterization

Glass Mountain pumices exhibit a range of vesicularities typical of rhyolite material. Total vesicularities represent 55–90 vol.% (average 74 vol.%), and connected vesicularities 45–85 vol.% (average 63 vol.%) of the sample volume. The pumice clasts have an average connected-to-total vesicularity ratio of 85%, which is typical for subplinian pumice (Table 2; Colombier et al., 2017; Thomas et al., 1994) and in agreement with previously published values for pumice clasts of the same eruptive units (Gonnermann et al., 2017). The analyzed clasts have an average bulk density of  $630 \text{ kg/m}^3$  and a DRE density of  $2,390 \text{ kg/m}^3$ , similar to previously reported values (Giachetti et al., 2021). Samples prepared into cores for permeability analysis have Darcian permeability values of  $10^{-13}$  to  $10^{-11} \text{ m}^2$ , and non-Darcian permeability values of  $10^{-9}$  to  $10^{-7} \text{ m}$  (Table 2), also in agreement with the literature (Gonnermann et al., 2017). The sampled pumice comes from several fall deposits representing different periods of time during the eruption. The vesicularity, permeability, and density are consistent between the fall deposits, indicating that the pumices produced by this eruption represent the products of an eruption with minimal fluctuations in eruptive conditions. This makes the Glass Mountain pumice a relatively simple sample set to study the role of magnetic particles in the vesiculation of silicic magmas. Both whole and cored clasts were characterized using magnetic methods (Brachfeld et al., 2024) to determine whether increasing vesicularity or permeability influences the total magnetic content. The 14 S. vesicular obsidian pieces studied show a range of 69–82 vol.% for total vesicularity, with an average of 74 vol.% of the sample volume. The average bulk density of the S. vesicular obsidian pieces is  $636 \text{ kg/m}^3$ . The DRE is assumed to be  $2,430 \text{ kg/m}^3$ , the same as the obsidian reported by Giachetti et al. (2015).

#### 3.2. MELTS Modeling

Micron-scale magnetite crystals are observed in both the pumice (via X-ray computed tomography by Jessica Maisano at the University of Texas Computed Tomography laboratory) and obsidian (imaged via scanning

**Table 3**  
Maximum-Minimum Ranges of Volume % Titanomagnetite

Eruptive product	Average $k_{\text{ferro}}$ (SI)	Min volume (%)	Max volume (%)
Pumice	4.97E-05	0.0017	0.0080
Northern Obsidian	1.92E-05	0.0006	0.0031
Southern Obsidian	9.38E-05	0.0031	0.0151
Southern Vesicular Obsidian	1.02E-04	0.0034	0.0165

electron microscopy by Francisco Cáceres at the University of München) but in relatively low volumetric quantities and numerical crystal abundances (Figure S1 in Supporting Information S1). Did these crystals form during magma ascent or did they exist in the magma prior to its eruption? Chemical modeling (MELTS; Ghiorso & Gualda, 2015; Gualda et al., 2012) is used to evaluate the likelihood that Glass Mountain magma contained magnetite prior to eruption by evaluating its thermodynamic stability at relevant magma storage conditions (Grove et al., 1997). Modeling reveals that magnetite saturation occurs at 749°C at  $f\text{O}_2$  corresponding to FMQ reaction buffer, 827°C at NNO (i.e., FMQ + 0.5) and 900°C at FMQ + 2. This result is corroborated by the presence of spinel in experimental runs performed at 880–1000°C,  $f\text{O}_2$  corresponding to NNO, and 100 MPa at  $\text{H}_2\text{O}$  saturation on putative parental materials (Grove et al., 1997). Moreover, coexisting Fe-Ti oxides in the obsidian indicate that pre-eruption temperature and  $f\text{O}_2$  (expressed as  $\Delta\text{FMQ}$ ) of the rhyolite magma range from 900 to 980°C and 0.7–2.1, respectively (Carmichael, 1967, 1991). Thermodynamic modeling, together with experimental constraints and Fe-Ti thermobarometry, supports the petrographic observation of magnetite and suggests that the Glass Mountain rhyolite contained magnetite crystals prior to ascent.

### 3.3. Magnetic Mineral Characterization

Brachfeld et al. (2024) present detailed room temperature and high temperature analyses that constrain titanomagnetite mineralogy and domain state. A summary is given here. Glass Mountain pumice, obsidian, and vesicular obsidian acquire an anhysteretic remanent magnetization whose intensity is dependent on the applied field bias strength ( $H_{\text{DC}}$ ). This indicates the presence of a remanence-carrying mineral, necessitating that a portion of the grain size distribution is within the SSD or larger size range, >50–80 nm for magnetite and titanomagnetite. In pumice samples, a portion of the grain size distribution is also superparamagnetic (SP, <50–80 nm), as evidenced by very low coercivities ( $H_{\text{C}}$ ) and very low remanence ratios ( $M_{\text{R}}/M_{\text{S}}$ ) observed during hysteresis measurements, and by room temperature frequency-dependence of magnetic susceptibility (Brachfeld et al., 2024). Glass Mountain obsidian hysteresis parameters are generally more SSD-like, though with some SP content. The titanomagnetite composition determined from thermomagnetic analyses is variable, ranging from  $\text{Fe}_3\text{O}_4$  to  $\text{Fe}_{2.4}\text{Ti}_{0.6}\text{O}_4$ . Minimum and maximum values of titanomagnetite volume fraction were determined by dividing the average volume-normalized ferromagnetic susceptibility ( $k_{\text{ferro}}$ ) of each eruptive product by the susceptibilities of  $\text{Fe}_3\text{O}_4$  (3 SI) and  $\text{Fe}_{2.4}\text{Ti}_{0.6}\text{O}_4$  (0.62 SI). Volume fraction was then converted to volume % (v%). Both eruptive and effusive products contain titanomagnetite with a range of magnetic domain states spanning SP through MD. Titanomagnetite v% ranges overlap for all eruptive and effusive products (Table 3).

### 3.4. Low Temperature Remanence Behavior

Samples that display room temperature signatures of superparamagnetism were selected for low-temperature field-cooled zero-field cooled (FC-ZFC) remanence experiments. We observed three types of results: (type 1) samples for which the ZFC curve is stronger than the FC curve, consistent with low temperature observations of MD magnetite (Brachfeld et al., 2001, 2002; Carter-Stiglitz et al., 2006; Figure 3a); (type 2) samples that display an order-disorder transition at ~55–65 K, consistent with MD titanomagnetite and other cation-substituted iron oxides (Brachfeld & Hammer, 2006; Moskowitz et al., 1998) (Figures 3a–3c); (type 3) samples for which the FC curve is stronger than the ZFC curve, consistent with SSD titanomagnetite (Moskowitz et al., 1993) (Figures 3d–3f). MD signals dominate type 1 and type 2 behavior and overwhelm nanoparticle signatures. Therefore, only type 3 samples, which lack MD features and lack the 55–65 K feature (checked by observing the first derivative of the  $M_{\text{R}}\text{-T}$  curve), were used to calculate grain size distributions (Figures 3d–3f).

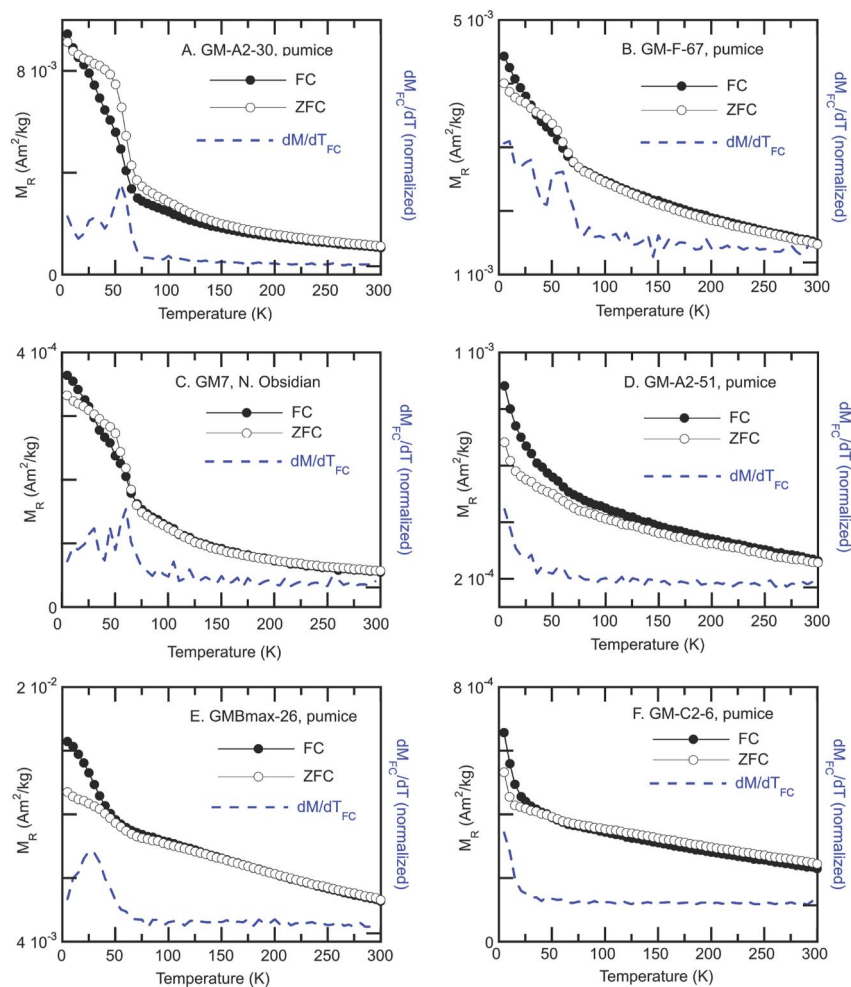


**Figure 3.** Low-temperature field-cooled zero-field cooled (FC-ZFC) results for pumice and obsidian. Some samples that show SP characteristics at room temperature are dominated by multidomain characteristics in the FC-ZFC experiment (a–c). Samples whose low temperature FC-ZFC profiles have stable single domain characteristics and for which crystallographic transitions are absent in the first derivative of the field cooled curve (d–f) are candidates for determining grain size distribution according to Wörm and Jackson (1999).

### 3.5. Blocking Volume Approximation and Number Density

The FC curves for three pumice samples were used to determine titanomagnetite blocking volumes, grain edge lengths (assuming cubic particles), and number densities using Equations 3 and 9 (Figure 4, Tables S1–S3). Grain edge lengths span approximately 3–33 nm. For each sample, we calculate the  $V_B$  distribution and TND assuming all particles are  $\text{Fe}_3\text{O}_4$  and a second time assuming all particles are titanomagnetite ( $\text{Fe}_{3-x}\text{Ti}_x\text{O}_4$ ), with the highest  $x$  parameter determined from the Curie temperature measurements. We use  $H_C$  (5 K) values of 10 and 100 mT for both compositions, which become  $H_k$  values of 16.6 and 166 kA/m, respectively. The pumice samples yield number densities of  $10^{18}$  to  $10^{20} \text{ m}^{-3}$ .

## 4. Discussion

In the following sections, we discuss the magnetic characteristics of the pumice and obsidian and compare quantities of magnetic crystals with quantities of vesicles in the framework of heterogeneous nucleation. We then consider the timing of titanomagnetite formation over the magma storage, ascent, and eruption history and evaluate the impacts of this study on the use of decompression rate meters and conduit models.

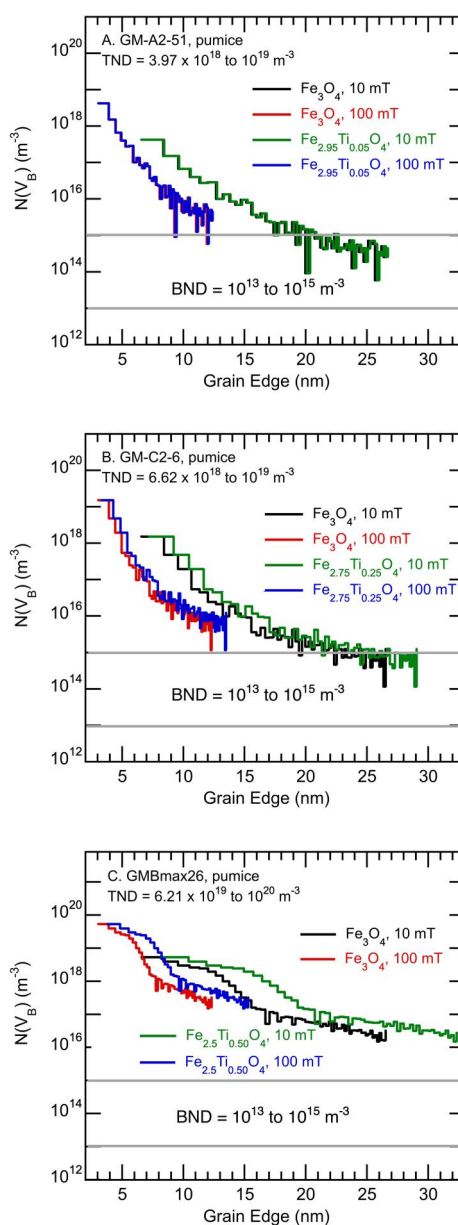


**Figure 4.** The method described in Wörm and Jackson (1999) was applied to determine the number of titanomagnetite particles in each size bin per  $\text{m}^3$  of sample ( $N(V_B)$ ) for (a) GM-A2-51 pumice, (b) GM-C2-6 pumice, and (c) GMBmax26 pumice. For each pumice specimen, we explored the effects of composition and macrocoercivity ( $H_C$ , from which microcoercivity  $H_k$  is determined) variations. Black and red curves were calculated assuming that all particles have composition  $\text{Fe}_3\text{O}_4$ . Green and blue curves were calculated assuming that all particles have composition  $\text{Fe}_{3-x}\text{Ti}_x\text{O}_4$  using the most Ti-rich composition (the highest  $x$  parameter) observed in Curie temperature measurements (Brachfeld et al., 2024). The smallest  $V_B$  detected using this method is constrained by the temperature at which the remanence is imparted, 5 K for this study. The largest  $V_B$  is constrained by the highest blocking temperature ( $T_B$ ) for the coarsest SP particles in the assemblage. The DRE-adjusted TNDs in Glass Mountain pumice,  $10^{18}$  to  $10^{20} \text{ m}^{-3}$  for these specimens, are several orders of magnitude greater than the range of bubble number densities for Glass Mountain pumice ( $10^{13}$  to  $10^{15} \text{ m}^{-3}$ ; Giachetti et al., 2015).

#### 4.1. Presence and Abundance of Nano to Micron Scale Titanomagnetite in Pumice and Obsidian

Using the Wörm and Jackson (1999) method, blocking volume measurements at a range of temperatures from 5 K to room temperature yielded magnetic particle sizes of 3–33 nm in diameter in the Glass Mountain pumice. This method assumes that magnetization changes from paramagnetic ordering and IRM carried by MD grains is small compared with  $\Delta m_{\text{rs}}$  due to SP particles, which is reasonable given the absence of room-temperature MD

signatures in the selected samples. While these contributions, if present, would raise the TND, we note that this method does not detect coarse SP through SSD (up to 1,000 nm) and larger grains and so we consider our TND to be minima. The Wörm and Jackson (1999) method yields pumice TNDs that are similar to pumice and obsidian estimates derived from titanomagnetite vol.%, assuming a monospecific grain size assemblage for 1,000 to 10 nm particles ( $10^{12}$  to  $10^{20}$   $\text{m}^{-3}$ ) or a power law grain size distribution spanning 10 nm to 50  $\mu\text{m}$  ( $10^{18}$  to  $10^{19}$   $\text{m}^{-3}$ ) (Brachfeld et al., 2024). We therefore consider the TND range of  $10^{18}$  to  $10^{20}$   $\text{m}^{-3}$  to be robust. Magnetic methods allow us to resolve the titanomagnetite in silicate glass within a size range below the detection limits of conventional imaging techniques (petrographic and field emission gun electron microscopy, X-ray tomography).

#### 4.1.1. Is Titanomagnetite Abundant Enough to Fully Foster Heterogeneous Bubble Nucleation?

Using a combination of 3D microtomography and 2D textural data, Burgisser et al. (2020) recently discussed the extent to which oxides affect the efficiency of bubble nucleation, distinguishing three scenarios: (a) oxides outnumber vesicles, (b) oxides and vesicles are roughly equally abundant, and (c) vesicles outnumber oxides. The first two scenarios likely imply that fully heterogeneous bubble nucleation is possible, while the third scenario leaves the possibility of hybrid homogeneous-heterogeneous nucleation during degassing. They further showed that beyond the relative abundance of oxides and vesicles, assessing their textural relationship (adjoined or isolated) was important in determining the dominant nucleation mechanism, particularly in cases where vesicles are equally or more abundant than oxides. In Glass Mountain pumice, the calculated TNDs ( $10^{18}$  to  $10^{20}$   $\text{m}^{-3}$ ) exceed BNDs by several orders of magnitude (BND on the order of  $10^{13}$  to  $10^{15}$   $\text{m}^{-3}$ ; Giachetti et al., 2015; Trafton & Giachetti, 2021). Comparable magnetic susceptibility values and vol.% titanomagnetite in both the pumice and obsidian samples suggest that titanomagnetite was present over the duration of the eruption, both in the early explosive phase (producing the pumice) and the later effusive. The titanomagnetite present in the Glass Mountain pumice and obsidian is therefore present and in abundances great enough to fully foster heterogeneous bubble nucleation in this eruption. Magnetic techniques allowed us to access the nm-scale and could prove essential in re-assessing the respective abundances of oxides and vesicles in samples from other eruptions of differing styles and magma compositions (e.g., Burgisser et al., 2020). Whether fully heterogeneous nucleation dominates in nature or whether nucleation is, in certain cases, hybrid (both heterogeneous and homogeneous, e.g., Gardner et al., 2023) will best be ascertained by integrating traditional sample imaging techniques and magnetic measurements. Current applications of X-ray computed tomography can successfully detect micron scale objects and provide 3D textural context (e.g., Giachetti et al., 2011; Gualda & Rivers, 2006), whereas magnetic methodologies excel at the detection of nm scale oxides. Combining magnetic methodologies and X-ray computed tomography scans bridges the detection limit gap of the two methods and finally provides a new path toward characterizing the relationship between bubble nucleation and titanomagnetite.

#### 4.2. What Is the Timing of Titanomagnetite Formation?

Titanomagnetite must be present prior to vesiculation in order to act as a heterogeneous nucleation site for bubbles. To investigate whether titanomagnetite crystals predate bubble nucleation and are not a result of post-eruption oxidation or syn-ascent permeable gas fluxing, we compare the magnetic and textural properties of obsidian and pumice. The N. obsidian and S. obsidian samples represent a fully outgassed magma whose bubble framework has disappeared. Pumice, on the other hand, is a record of vesicularity, permeability, and bubble number density near the fragmentation level. The S. vesicular obsidian represents a lava flow sample that still preserves a significant bubble framework and provides an opportunity for a textural comparison to the pumice. All three sample types originated from the same magma reservoir, started with the same chemical compositions and presumably water contents, and only differed in their outgassing history. If titanomagnetite formed before magma ascent, degassing and outgassing, it should be in similar abundance within the dense obsidians, vesicular obsidian, and the pumice. By assessing the presence and abundance of titanomagnetite crystals in both obsidian and pumice, we can test if titanomagnetite formation is independent of the development of vesicularity and permeable pathways and rule out the formation of titanomagnetite as a result of post- or syn-eruptive oxidation.

Here, we use magnetic susceptibility as a proxy for magnetic mineral abundance and compare it with vesicularity and permeability to investigate the timing of titanomagnetite nucleation. As air-filled void space will act as a “dilutant” and decrease volume-normalized susceptibility ( $k$ ), we conduct this test using mass-normalized susceptibility ( $\chi$ ) to ensure that any trends are solely due to the properties of the solids. There was no correlation between susceptibility and vesicularity or permeability (Figures 5a–5c), indicating that the formation of

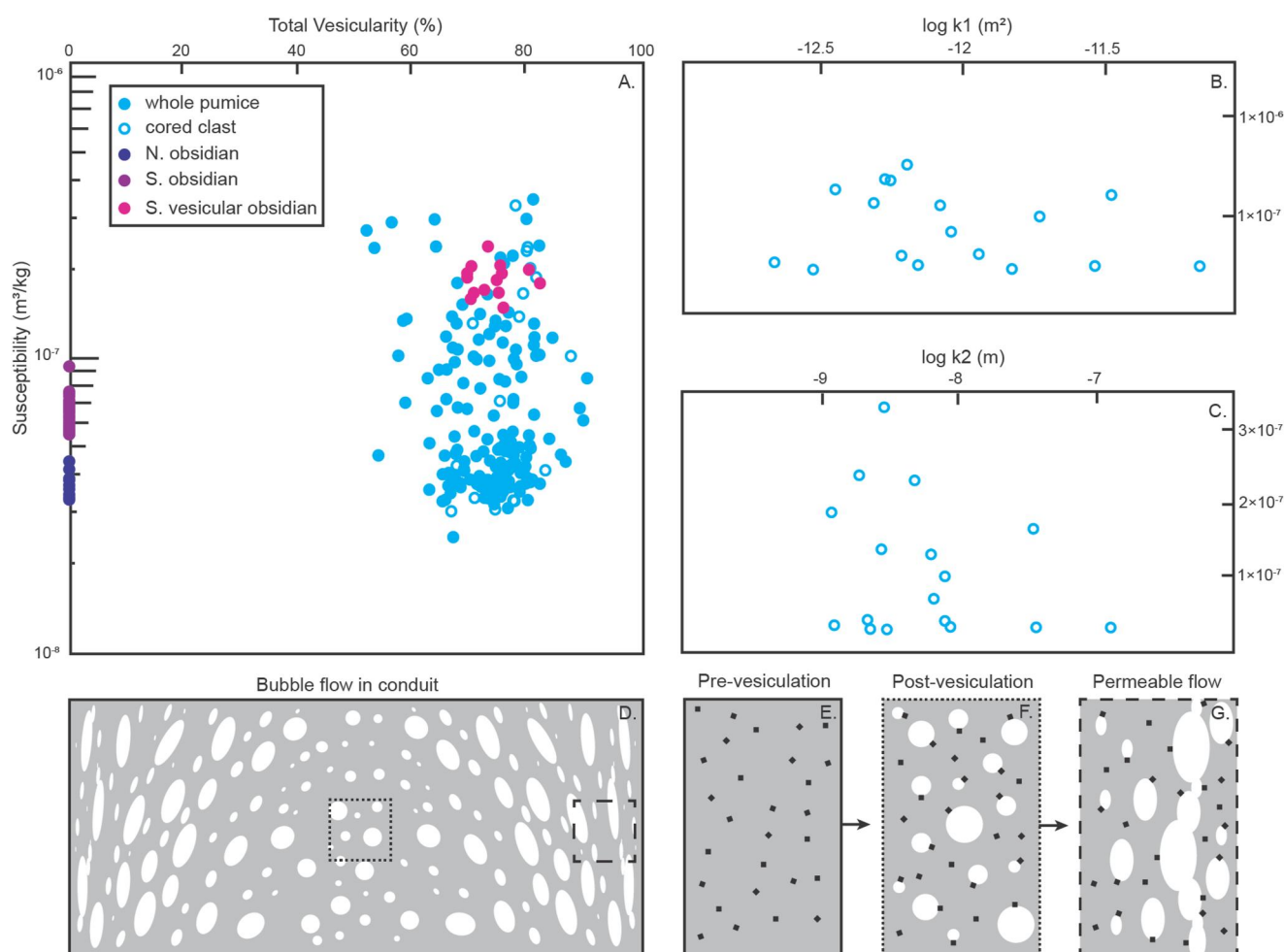


**Figure 5.** Mass-normalized magnetic susceptibility ( $\chi$ ) versus total vesicularity and permeability for individual pumice clasts (cored and whole). (a–c) There are no discernible trends in increasing vesicularity or permeability with susceptibility. In addition, N. obsidian, S. obsidian, and S. vesicular flow samples overlap with the majority of pumice samples, indicating that titanomagnetite abundance is similar between the range of samples analyzed. (d–g) This indicates that titanomagnetite was likely an early forming mineral phase that could act as a heterogeneous nucleation site, and vesiculation and development of permeable pathways did not form titanomagnetite as a result of oxidation.

titanomagnetite was not contingent upon the development of bubbles or permeable pathways. In addition, N. obsidian, S. obsidian, and S. vesicular flow samples overlap with the majority of pumice samples, indicating that titanomagnetite abundance is similar across the explosive and effusive eruption styles represented by the samples analyzed.

The comparable susceptibility ranges detected for Glass Mountain pumice, N. obsidian, S. obsidian, and S. vesicular obsidian, as well as the lack of correlation between vesicularity and permeability with susceptibility indicate that titanomagnetite most likely was unaffected by gas circulation in a permeable magma. That is, titanomagnetite was likely present prior to vesiculation (Figure 5e) in all ascending magma, and thus available to act as heterogeneous nucleation sites for bubbles. The presence of magnetite in both low-permeability pumice (Figure 5f) as well as high-permeability pumice (i.e., at highly sheared areas of the conduit, Figure 5g) is therefore not contingent upon gas circulation through (and oxidation of) gas-permeable magma (Figure 5d). In addition, MELTS modeling affirms early titanomagnetite stability in the Glass Mountain system, supporting the likelihood that titanomagnetite formed prior to the eruption. This relative timing is corroborated by additional lines of evidence, including vesicularity-independent magnetic susceptibility and an observed anisotropy of magnetic susceptibility (Brachfeld et al., 2024), in which the highest degree of anisotropy coincides with high vesicularity. Degassing, outgassing of magma, and the cooling history of the samples at the surface are therefore unrelated to titanomagnetite formation, and the magnetite particles were available in abundance prior to vesiculation.

### 4.3. What Changes if nm-Scale Titanomagnetite Acts as a Heterogeneous Nucleation Mechanism?

This study shows that nm-scale titanomagnetite is present in number densities greater than BND in the studied pumice and obsidian of the 1060 CE Glass Mountain eruption. With new applications of magnetic methodologies, we now need to reevaluate the bubble nucleation style that occurs in similar systems, as the presence of abundant nm-scale magnetic particles would change the application of decompression rate meters and help reconcile BND and eruption dynamics in previously identified “homogeneous” systems.

Bubble nucleation is the dominant control on degassing efficiency. Current decompression rate meters (Toramaru, 1989, 1995, 2006) and conduit models (Gonnermann & Houghton, 2012) based on classical nucleation theory or its derivatives yield results that depend disproportionately on the choice of a value for vapor-liquid surface tension ( $\sigma_{MB}$ ). The value of  $\sigma_{MB}$  is 0.06–0.1 N/m if homogeneous nucleation takes place, and 0.01–0.04 N/m if heterogeneous nucleation takes place. Decompression rates can vary by orders of magnitude depending on this choice (Shea, 2017). “Effective” values for surface tension have largely been extracted using bubble textures produced in laboratory decompression experiments, both for oxide-bearing and oxide-free melts (e.g., Cluzel et al., 2008; Gardner & Ketcham, 2011; Hurwitz & Navon, 1994; Mangan & Sisson, 2005) thought to foster heterogeneous and homogeneous bubble nucleation respectively. The relationship between the decompression rate and measured BNDs within these two groups of experiments is not always obvious and calculated surface tensions display substantial scatter even for similar experimental starting compositions and decompression strategies (Fiege & Cichy, 2015). Explanations for experimental discrepancies have often focused on the role of cryptic melt structure, atomic clusters, or unresolved oxides in the starting material that may be present or absent depending on super- or sub-liquidus annealing of experimental charges prior to decompression (Hurwitz & Navon, 1994; Larsen, 2008; Preuss et al., 2016; Shea, 2017). Magnetic techniques could be applied both in pre- and post-decompression experimental charges to carefully test whether cryptic variations in oxide abundance are responsible for the scattering in key nucleation parameters.

The presence of nanolites prior to bubble nucleation has ramifications for our understanding of volcanic conduit processes through their influence on liquid and magma viscosity, the timing of volatile exsolution (through influence on bubble nucleation), the concentrations of dissolved volatiles and ultimately, the rheology of magma as a multiphase fluid. These interrelated consequences of nanolites exert a complex influence on the ascent rate and thus the explosivity of magma. For example, Di Genova et al. (2020) and Cáceres et al. (2020) examine the role of nanolites in the evolution of a magmatic system. If they facilitate bubble nucleation, even dense titanomagnetite nanolites drive a tremendous increase in magma buoyancy, which causes magma ascent to accelerate (Cáceres et al., 2020, 2022). The decrease in the dissolved volatile content increases the liquid viscosity, moving the system toward the viscous-brittle regime (Cáceres et al., 2020, 2024). Compounding this effect, the formation of titanomagnetite locally increases the liquid SiO<sub>2</sub> content and thus increases the liquid viscosity. Both factors push the system closer to the viscous-brittle regime and explosive eruption.

## 5. Conclusions

The results of our magnetic characterization resolve the observational inconsistency associated with heterogeneous bubble nucleation by expanding the realm of direct titanomagnetite observation toward sub-microscopic (i.e., nm) sizes. Rhyolitic pumice from the 1060 CE Glass Mountain subplinian eruption contains titanomagnetite ultrananolites with  $10^{18}$  to  $10^{20}$  m<sup>-3</sup> in the 3–33 nm size range, comparable to TNDs determined for obsidian and vesicular obsidian via room temperature methods. These number densities are interpreted as minima, and so the TND present in the obsidian and pumice therefore far exceeds the BND range of Glass Mountain pumice ( $10^{13}$  to  $10^{15}$  m<sup>-3</sup>; Trafton & Giachetti, 2021). Thus, titanomagnetite crystals are numerically abundant in both pumice and obsidian, and occur in quantities that are sufficient to serve as heterogeneous nucleation substrates for every bubble in the quenched pumice.

Comparable number densities alone are insufficient to support a causation relationship between crystals and bubbles; crystals must precede the bubble formation in order to exert an influence on the bubble formation. The results of our textural characterization and petrologic (MELTS) modeling are consistent with the appearance of titanomagnetite crystals before the appearance of bubbles.

Our detection of nm-scale titanomagnetite crystals in the products of eruptions previously thought to be driven by homogeneous bubble nucleation should refocus attention on studies of other eruptions, particularly those that do

not meet the criteria consistent with homogeneous nucleation (e.g., Hajimirza et al., 2021; Shea, 2017). Magnetic techniques provide a means to identify the presence of nanometer scale heterogeneous nucleation sites in erupted material. The methodologies described herein and in Brachfeld et al. (2024) permit critical evaluation of the potential role of titanomagnetite in bubble nucleation, with implications for the application of BND-based decompression rate meters (e.g., Toramaru, 1989, 1995, 2006), and viscosity parameters in eruption models (Cáceres et al., 2020, 2024; Di Genova et al., 2020).

### Data Availability Statement

Low-temperature remanence data and room-temperature magnetic susceptibility data are archived through the Magnetics Information Consortium Database at <https://doi.org/10.7288/V4/MAGIC/20019> and <https://doi.org/10.7288/V4/MAGIC/20020>, respectively. Physical Characterization data of the pumice (i.e., mass, density, vesicularity, and permeability) are archived at (McCartney, 2024) <https://hdl.handle.net/10125/107683>.

### Acknowledgments

This work was funded by National Science Foundation Grants 1839230 to Hammer and Shea and 1839313 to Brachfeld. We thank the members of the Institute for Rock Magnetism for kindly conducting analyses prior to our team's visit and for their support and discussions during our team's visit. SB thanks Mike Jackson for helpful discussions. The IRM is made possible through the Instrumentation and Facilities program of the National Science Foundation Grants 1642268 and 2153786 and by funding from the University of Minnesota. We thank Jessica Maisano and the members of the High-Resolution X-ray computed tomography facility (UTCT) for their imaging of the Glass Mountain pumice (NSF EAR-1762458; NASA 80NSSC23K0199). This imaging was performed in association with the UTCT hosted a workshop of the ToScANA North America conference of Summer 2021. We thank Francisco Cáceres for the scanning electron microscopy imaging of the Glass Mountain pumice at the University of München. We thank Allan Lerner at the University of Oregon for FTIR analysis of Glass Mountain obsidian, and Melissa Hansen for assistance with magnetic susceptibility measurements at Montclair State University. We thank Brendan Cych and an anonymous reviewer for their constructive comments that improved this manuscript, and Associate Editor Joshua Feinberg for administrative handling of this manuscript.

### References

- Berndt, T., Muxworthy, A. R., & Paterson, G. A. (2015). Determining the magnetic attempt time  $\tau_0$ , its temperature dependence, and the grain size distribution from magnetic viscosity measurements. *Journal of Geophysical Research: Solid Earth*, 120(11), 7322–7336. <https://doi.org/10.1002/2015JB012283>
- Bleil, U., & Petersen, N. (1982). Magnetic properties of natural minerals. In G. Angenheister (Ed.), *Numerical Data and Functional Relationships in Science and Technology, Group V: Geophysics and Space Research* (pp. 308–365). Springer.
- Brachfeld, S., Banerjee, S. K., Guyodo, Y., & Acton, G. D. (2002). A 13,200 year history of century to millennial scale paleoenvironmental change magnetically recorded in the Palmer Deep, western Antarctic Peninsula. *Earth and Planetary Science Letters*, 194(3–4), 311–326. [https://doi.org/10.1016/S0012-821X\(01\)00567-2](https://doi.org/10.1016/S0012-821X(01)00567-2)
- Brachfeld, S., Guyodo, Y., & Acton, G. D. (2001). The magnetic mineral assemblage of hemipelagic drifts, ODP Site 1096. In P. F. Barker, A. Camerlenghi, G. D. Acton, & A. T. S. Ramsay (Eds.), *Proceeding of the Ocean Drilling Program Scientific Results* (p. 178). Retrieved from [http://www.odp.tamu.edu/publications/178\\_SR/VOLUME/CHAPTERS/SR178\\_14.PDF](http://www.odp.tamu.edu/publications/178_SR/VOLUME/CHAPTERS/SR178_14.PDF)
- Brachfeld, S., & Hammer, J. (2006). Rock-magnetic and remanence properties of synthetic Fe-rich basalts: Implications for Mars crustal anomalies. *Earth and Planetary Science Letters*, 248(3–4), 599–617. <https://doi.org/10.1016/j.epsl.2006.04.015>
- Brachfeld, S., McCartney, N. K., Hammer, J., Shea, T., & Giachetti, T. (2024). Titanomagnetite nanolites and ultrananolites: An abundant and early-forming component of aphyric rhyolitic pumice and obsidian from Glass Mountain, California. *Geochemistry, Geophysics, Geosystems*, 25, e2023GC011336. <https://doi.org/10.1029/2023GC011336>
- Buckland, H. M., Cachman, K. V., Engwell, S. L., & Rust, A. C. (2020). Sources of uncertainty in the Mazama isopachs and the implications of interpreting distal tephra deposits from large magnitude eruptions. *Bulletin of Volcanology*, 82, 1–17. <https://doi.org/10.1007/s00445-020-1362-1>
- Burgisser, A., Alletti, M., & Scaillet, B. (2015). Simulating the behavior of volatiles belonging to the C–O–H–S system in silicate melts under magmatic conditions with the software D-Compress. *Computers & Geosciences*, 79, 1–14. <https://doi.org/10.1016/j.cageo.2015.03.002>
- Burgisser, A., Arbaret, L., Martel, C., Forien, M., & Colombier, M. (2020). The role of oxides in the shallow vesiculation of ascending magmas. *Journal of Volcanology and Geothermal Research*, 406, 107072–107087. <https://doi.org/10.1016/j.jvolgeores.2020.107072>
- Butler, R. F. (1992). *Paleomagnetism: Magnetic domains to geologic terranes, Chapter 2: Ferrimagnetic Minerals* (pp. 16–30). Blackwell Scientific Publications.
- Cáceres, F., Hess, K. U., Eitel, M., Döblinger, M., McCartney, K. N., Colombier, M., et al. (2024). Oxide nanolite-induced melt iron extraction causes viscosity jumps and enhanced explosivity in silicic magma. *Nature Communications*, 15, 1–11. <https://doi.org/10.1038/s41467-024-44850-x>
- Cáceres, F., Scheu, B., Colombier, M., Hess, K., Feisel, Y., Ruthensteiner, B., & Dingwell, D. B. (2022). The roles of microlites and phenocrysts during degassing of silicic magma. *Earth and Planetary Science Letters*, 577, 117264. <https://doi.org/10.1016/j.epsl.2021.117264>
- Cáceres, F., Wadsworth, F. B., Scheu, B., Colombier, M., Madonna, C., Cimarelli, C., et al. (2020). Can nanolites enhance eruption explosivity? *Geology*, 48(10), 997–1001. <https://doi.org/10.1130/G47317.1>
- Carmichael, I. S. E. (1967). The iron-titanium oxides of silic volcanic rocks and their associated ferromagnesian silicates. *Contributions to Mineralogy and Petrology*, 14(1), 36–64. <https://doi.org/10.1007/BF00370985>
- Carmichael, I. S. E. (1991). The redox states of basic and silicic magmas: A reflection of their source regions? *Contributions to Mineralogy and Petrology*, 106(2), 129–141. <https://doi.org/10.1007/BF00306429>
- Carter-Stiglitz, B., Moskowitz, B., Sølheid, P., Berquó, T. S., Jackson, M., & Kosterov, A. (2006). Low-temperature magnetic behavior of multidomain titanomagnetites: TM0, TM16, and TM35. *Journal of Geophysical Research*, 111(B12), B12S05. <https://doi.org/10.1029/2006JB004561>
- Clark, H. A. (2012). *Evolution of volatile content of the parent magma of the 1875 eruption of Askja volcano, Iceland* Masters Thesis 1911. University of Massachusetts Amherst. <https://doi.org/10.7275/2685364>
- Cluzel, N., Laporte, D., Provost, A., & Kannevischer, I. (2008). Kinetics of heterogeneous bubble nucleation in rhyolitic melts: Implications for the number density of bubbles in volcanic conduits and for pumice textures. *Contributions to Mineralogy and Petrology*, 156(6), 745–763. <https://doi.org/10.1007/s00410-008-0313-1>
- Colombier, M., Wadsworth, F. B., Gurioli, L., Scheu, B., Kueppers, U., Muro, A. D., & Dingwell, D. B. (2017). The evolution of pore connectivity in volcanic rocks. *Earth and Planetary Science Letters*, 462, 99–109. <https://doi.org/10.1016/j.epsl.2017.01.011>
- Colombier, M., Wadsworth, F. B., Scheu, B., Vasseur, J., Dobson, K. J., Cáceres, F., et al. (2020). In situ observation of the percolation threshold in multiphase magma analogues. *Bulletin of Volcanology*, 82(4), 32–47. <https://doi.org/10.1007/s00445-020-1370-1>
- Coombs, M. L., & Gardner, J. E. (2001). Shallow-storage conditions for the rhyolite of the 1912 eruption at Novarupta, Alaska. *Geological Society of America*, 29(9), 775–778. [https://doi.org/10.1130/0091-7613\(2001\)029%3C0775:SSCFTR%3E2.0.CO;2](https://doi.org/10.1130/0091-7613(2001)029%3C0775:SSCFTR%3E2.0.CO;2)
- Dickson, D., Reid, B., Hunt, C., Williams, H., El-Hilo, M., & O'Grady, K. (1993). Determination of  $f_0$  for fine magnetic particles. *Journal of Magnetism and Magnetic Materials*, 125(3), 345–350. [https://doi.org/10.1016/0304-8853\(93\)90109-F](https://doi.org/10.1016/0304-8853(93)90109-F)

- Di Genova, D., Brooker, R. A., Mader, H. M., Drewitt, J. W. E., Longo, A., Deubener, J., et al. (2020). In situ observations of nanolite growth in volcanic melt: A driving force for explosive eruptions. *Science Advances*, 6(39), 1–15. <https://doi.org/10.1126/sciadv.abb0413>
- Dunbar, N., & Kyle, P. (1993). Lack of volatile gradient in the Taupo plinian-ignimbrite transition: Evidence from melt inclusion analysis. *American Mineralogist*, 78, 612–618.
- Dunlop, D. J., & Özdemir, Ö. (1997). *Rock magnetism: Fundamentals and frontiers* (Vol. 3). Cambridge University Press. <https://doi.org/10.1029/97JB02478>
- Fiege, A., & Cichy, S. B. (2015). Experimental constraints on bubble formation and growth during magma ascent: A review. *American Mineralogist*, 100(11–12), 2426–2442. <https://doi.org/10.2138/am-2015-5296>
- Formenti, Y., & Druitt, T. H. (2003). Vesicle connectivity in pyroclasts and implications for the fluidization of fountain-collapse pyroclastic flows, Montserrat (West Indies). *Earth and Planetary Science Letters*, 214(3–4), 561–574. [https://doi.org/10.1016/S0012-821X\(03\)00386-8](https://doi.org/10.1016/S0012-821X(03)00386-8)
- Gardner, J. E. (2007). Heterogeneous bubble nucleation in highly viscous silicate melts during instantaneous decompression from high pressure. *Chemical Geology*, 236(1–2), 1–12. <https://doi.org/10.1016/j.chemgeo.2006.08.006>
- Gardner, J. E., & Denis, M. H. (2004). Heterogeneous bubble nucleation on Fe-Ti oxide crystals in high-silica rhyolitic melts. *Geochimica et Cosmochimica Acta*, 68(17), 3587–3597. <https://doi.org/10.1016/j.gca.2004.02.021>
- Gardner, J. E., & Ketcham, R. A. (2011). Bubble nucleation in rhyolite and dacite melts: Temperature dependence of surface tension. *Contributions to Mineralogy and Petrology*, 162(5), 929–943. <https://doi.org/10.1007/s00410-011-0632-5>
- Gardner, J. E., Wadsworth, F. B., Carley, T. L., Llewellyn, E. W., Kusumaatmaja, H., & Sahagian, D. (2023). Bubble Formation in magma. *Annual Review of Earth and Planetary Sciences*, 51(1), 131–154. <https://doi.org/10.1146/annurev-earth-031621-080308>
- Ghiorso, M. S., & Gualda, G. A. R. (2015). An H<sub>2</sub>O-CO<sub>2</sub> mixed fluid saturation model compatible with rhyolite-MELTS. *Contributions to Mineralogy and Petrology*, 169(53), 1–30. <https://doi.org/10.1007/s00410-015-1141-8>
- Giachetti, T., Burgisser, A., Arbaret, L., Druitt, T. H., & Kelfoun, K. (2011). Quantitative textural analysis of Vulcanian pyroclasts (Montserrat) using multi-scale X-ray computed tomography: Comparison with results from 2D image analysis. *Bulletin of Volcanology*, 73(9), 1295–1309. <https://doi.org/10.1007/s00445-011-0472-1>
- Giachetti, T., Druitt, T. H., Burgisser, A., Arbaret, L., & Galven, C. (2010). Bubble nucleation, growth and coalescence during the 1997 Vulcanian explosions of Soufrière Hills Volcano, Montserrat. *Journal of Volcanology and Geothermal Research*, 193(3–4), 215–231. <https://doi.org/10.1016/j.jvolgeores.2010.04.001>
- Giachetti, T., Gonnermann, H. M., Gardner, J. E., Shea, T., & Gouldstone, A. (2015). Discriminating secondary from magmatic water in rhyolitic matrix-glass of volcanic pyroclasts using thermogravimetric analysis. *Geochimica et Cosmochimica Acta*, 148, 457–476. <https://doi.org/10.1016/j.gca.2014.10.017>
- Giachetti, T., Hudak, M. R., Shea, T., Bindeman, I. N., & Hossie, E. C. (2020). D/H ratios and H<sub>2</sub>O contents record degassing and rehydration history of rhyolitic magma and pyroclasts. *Earth and Planetary Science Letters*, 530, 115909–115923. <https://doi.org/10.1016/j.epsl.2019.115909>
- Giachetti, T., Trafton, K. R., Wiejaczka, J., Gardner, J. E., Watkins, J. M., Shea, T., & Wright, H. M. N. (2021). The products of primary magma fragmentation finally revealed by pumice agglomerates. *The Geological Society of America*, 49(11), 1–5. <https://doi.org/10.1130/G48902.1>
- Gonnermann, H. M., Giachetti, T., Fliedner, C., Nguyen, C. T., Houghton, B. F., Crozier, J. A., & Carey, R. J. (2017). Permeability during magma expansion and compaction. *Journal of Geophysical Research: Solid Earth*, 122(12), 9825–9848. <https://doi.org/10.1002/2017JB014783>
- Gonnermann, H. M., & Houghton, B. F. (2012). Magma degassing during the Plinian eruption of Novarupta Alaska, 1912. *Geochemistry, Geophysics, Geosystems*, 13(10), Q10009. <https://doi.org/10.1029/2012GC004273>
- Grove, T. L., Donnelly-Nolan, J. M., & Housh, T. (1997). Magmatic processes that generated the rhyolite of Glass Mountain, Medicine Lake Volcano, N. California. *Contributions to Mineralogy and Petrology*, 127(3), 205–223. <https://doi.org/10.1007/S004100050276>
- Gualda, G. A. R., Ghiorso, M. S., Lemons, R. V., & Carley, T. L. (2012). Rhyolite-MELTS: A modified calibration of MELTS optimized for silica-rich, fluid-bearing magmatic systems. *Journal of Petrology*, 53(5), 875–890. <https://doi.org/10.1093/petrology/egr080>
- Gualda, G. A. R., & Rivers, M. (2006). Quantitative 3D petrography using x-ray tomography: Application to Bishop Tuff pumice clasts. *Journal of Volcanology and Geothermal Research*, 154(1–2), 48–62. <https://doi.org/10.1016/j.jvolgeores.2005.09.019>
- Hajimirza, S., Gonnermann, H. M., & Gardner, J. E. (2021). Reconciling bubble nucleation in explosive eruptions with geospeedometers. *Nature Communications*, 12(1), 283–291. <https://doi.org/10.1038/s41467-020-20541-1>
- Heiken, G. (1978). Plinian-type eruptions in the Medicine Lake Highland, California, and the nature of the Underlying magma. *Journal of Volcanology and Geothermal Research*, 4(3–4), 375–402. [https://doi.org/10.1016/0377-0273\(78\)90023-9](https://doi.org/10.1016/0377-0273(78)90023-9)
- Hirth, J. P., Pound, G. M., & Pierre, G. R. S. (1970). Bubble nucleation. *Metallurgical Transactions A*, 1(4), 939–945. <https://doi.org/10.1007/BF02811776>
- Houghton, B. F., & Wilson, C. J. N. (1989). A vesicularity index for pyroclastic deposits. *Bulletin of Volcanology*, 51(6), 451–462. <https://doi.org/10.1007/BF01078811>
- Hurwitz, S., & Navon, O. (1994). Bubble nucleation in rhyolitic melts: Experiments at high pressure, temperature, and water content. *Earth and Planetary Science Letters*, 122(3–4), 267–280. [https://doi.org/10.1016/0012-821X\(94\)90001-9](https://doi.org/10.1016/0012-821X(94)90001-9)
- Klug, C., & Cashman, K. V. (1996). Permeability development in vesiculating magmas: Implications for fragmentation. *Bulletin of Volcanology*, 58(2–3), 87–100. <https://doi.org/10.1029/2011JB008494>
- Klug, C., Cashman, K. V., & Bacon, C. R. (2002). Structure and physical characteristics of pumice from the climactic eruption of Mount Mazama (Crater Lake), Oregon. *Bulletin of Volcanology*, 64(7), 486–501. <https://doi.org/10.1007/s00445-002-0230-5>
- Larsen, J. F. (2008). Heterogeneous bubble nucleation and disequilibrium H<sub>2</sub>O exsolution in Vesuvius K-phonolite melts. *Journal of Volcanology and Geothermal Research*, 175(3), 278–288. <https://doi.org/10.1016/j.jvolgeores.2008.03.015>
- Mandeville, C. W., Carey, S., Sigurdsson, H., & King, J. (1994). Paleomagnetic evidence for high-temperature emplacement of the 1883 subaqueous pyroclastic flows from Krakatau Volcano, Indonesia. *Journal of Geophysical Research*, 99(B5), 9487–9504. <https://doi.org/10.1029/94JB00239>
- Mangan, M., & Sisson, T. (2000). Delayed, disequilibrium degassing in rhyolite magma: Decompression experiments and implications for explosive volcanism. *Earth and Planetary Science Letters*, 183(3–4), 441–455. [https://doi.org/10.1016/S0012-821X\(00\)00299-5](https://doi.org/10.1016/S0012-821X(00)00299-5)
- Mangan, M., & Sisson, T. (2005). Evolution of melt-vapor surface tension in silicic volcanic systems: Experiments with hydrous melts. *Journal of Geophysical Research*, 110(B1), B01202. <https://doi.org/10.1029/2004JB003215>
- McCartney, K. (2024). McCartney et al., 2024 and Brachfeld et al., 2024 Pumice Physical Parameters [Dataset]. *ScholarSpace University of Hawai'i, Mānoa*. <https://hdl.handle.net/10125/107683>
- Moskowitz, B. M., Frankel, R. B., & Bazylinski, D. A. (1993). Rock magnetic criteria for the detection of biogenic magnetite. *Earth and Planetary Science Letters*, 120(3–4), 283–300. [https://doi.org/10.1016/0012-821X\(93\)90245-5](https://doi.org/10.1016/0012-821X(93)90245-5)

- Moskowitz, B. M., Frankel, R. B., Walton, S. A., Dickson, D. P., Wong, K., Douglas, T., & Mann, S. (1997). Determination of the preexponential frequency factor for superparamagnetic maghemite particles in magnetoferritin. *Journal of Geophysical Research*, *102*(97), 671–680. <https://doi.org/10.1029/97JB01698>
- Moskowitz, B. M., Jackson, M., & Kissel, C. (1998). Low-temperature magnetic behavior of titanomagnetites. *Earth and Planetary Science Letters*, *157*(3–4), 141–149. [https://doi.org/10.1016/S0012-821X\(98\)00033-8](https://doi.org/10.1016/S0012-821X(98)00033-8)
- Mourtada-Bonnefoi, C. C., & Laporte, D. (2002). Homogeneous bubble nucleation in rhyolitic magmas: An experimental study of the effect of H<sub>2</sub>O and CO<sub>2</sub>. *Journal of Geophysical Research*, *107*(B4), ECV 2-1–ECV 2-19. <https://doi.org/10.1029/2001JB000290>
- Néel, L. (1949). Théorie du trainage magnétique des ferromagnétiques en grains fins avec application aux terres cuites. *Annales de Geophysique*, *5*(2), 99–136.
- Preuss, O., Marxer, H., Ulmer, S., Wolf, J., & Nowak, M. (2016). Degassing of hydrous trachytic Campi Flegrei and phonolitic Vesuvius melts: Experimental limitations and chances to study homogeneous bubble nucleation. *American Mineralogist*, *101*(4), 859–875. <https://doi.org/10.2138/am-2016-5480>
- Rust, A. C., & Cashman, K. V. (2004). Permeability of vesicular silicic magma: Inertial and hysteresis effects. *Earth and Planetary Science Letters*, *224*(1–2), 93–107. <https://doi.org/10.1016/j.epsl.2004.09.025>
- Rust, A. C., & Cashman, K. V. (2011). Permeability controls on expansion and size distributions of pyroclasts. *Journal of Geophysical Research*, *116*(B11), B11202. <https://doi.org/10.1029/2011JB008494>
- Sahagian, D., & Proussevitch, A. (1998). 3D particle size distributions from 2D observations: Stereology for natural applications. *Journal of Volcanology and Geothermal Research*, *84*(3–4), 173–196. [https://doi.org/10.1016/S0377-0273\(98\)00043-2](https://doi.org/10.1016/S0377-0273(98)00043-2)
- Shea, T. (2017). Bubble nucleation in magmas: A dominantly heterogeneous process? *Journal of Volcanology and Geothermal Research*, *343*, 155–170. <https://doi.org/10.1016/j.jvolgeores.2017.06.025>
- Shea, T., Houghton, B. F., Gurioli, L., Cashman, K. V., Hammer, J. E., & Hobden, B. J. (2010). Textural studies of vesicles in volcanic rocks: An integrated methodology. *Journal of Volcanology and Geothermal Research*, *190*(3–4), 271–289. <https://doi.org/10.1016/j.jvolgeores.2009.12.003>
- Stoner, E. C., & Wohlfarth, E. P. (1948). A mechanism of magnetic hysteresis in heterogeneous alloys. *Philosophical Transactions of the Royal Society Series A*, *240*(826), 599–642. <https://doi.org/10.1098/rsta.1948.0007>
- Takeuchi, S., Nakashima, S., & Tomiya, A. (2008). Permeability measurements of natural and experimental volcanic materials with a simple permeameter: Toward an understanding of magmatic degassing processes. *Journal of Volcanology and Geothermal Research*, *177*(2), 329–339. <https://doi.org/10.1016/j.jvolgeores.2008.05.010>
- Takeuchi, S., Nakashima, S., Tomiya, A., & Hiroshi, S. (2005). Experimental constraints on the low gas permeability of vesicular magma during decompression. *Geophysical Research Letters*, *32*(10), L10312. <https://doi.org/10.1029/2005GL022491>
- Thomas, N., Jaupert, C., & Vergnolle, S. (1994). On the vesicularity of pumice. *Journal of Geophysical Research*, *99*(B8), 15633–15644. <https://doi.org/10.1029/94JB00650>
- Till, J. L., Jackson, M. J., Rosenbaum, J. G., & Solheid, P. (2011). Magnetic properties in an ash flow tuff with continuous grain size variation: A natural reference for magnetic particle granulometry. *Geochemistry, Geophysics, Geosystems*, *12*(7), Q07Z26. <https://doi.org/10.1029/2011GC003648>
- Toramaru, A. (1989). Vesiculation process and bubble size distributions in ascending magmas with constant velocities. *Journal of Geophysical Research*, *94*(B12), 17523–17542. <https://doi.org/10.1029/JB094iB12p17523>
- Toramaru, A. (1995). Numerical study of nucleation and growth of bubbles in viscous magmas. *Journal of Geophysical Research*, *100*(B2), 1913–1931. <https://doi.org/10.1029/94JB02775>
- Toramaru, A. (2006). BND (bubble number density) decompression rate meter for explosive volcanic eruptions. *Journal of Volcanology and Geothermal Research*, *154*(3–4), 303–316. <https://doi.org/10.1016/j.jvolgeores.2006.03.027>
- Trafton, K. R., & Giachetti, T. (2021). The morphology and texture of Plinian pyroclasts reflect their lateral sourcing in the conduit. *Earth and Planetary Science Letters*, *562*, 116844. <https://doi.org/10.1016/j.epsl.2021.116844>
- Wallace, P. J., Dufek, J., Anderson, A. T., & Zhang, Y. (2002). Cooling rates of Plinian-fall and pyroclastic-flow deposits in the Bishop Tuff: Inferences from water speciation in quartz-hosted glass inclusions. *Bulletin of Volcanology*, *65*(2–3), 105–123. <https://doi.org/10.1007/s00445-002-0247-9>
- Waters, L. E., & Lange, R. A. (2016). No effect of H<sub>2</sub>O degassing on the oxidation state of magmatic liquids. *Earth and Planetary Science Letters*, *447*, 48–59. <https://doi.org/10.1016/j.epsl.2016.04.030>
- Wörm, H. U., & Jackson, M. (1999). The superparamagnetism of Yucca Mountain Tuff. *Journal of Geophysical Research*, *104*(B11), 25415–25425. <https://doi.org/10.1029/1999JB900285>